Climate Data Record (CDR) Program

Climate Algorithm Theoretical Basis Document (C-ATBD)

VIIRS Leaf Area Index (LAI) and

Fraction of Absorbed Photosynthetically Active Radiation (FAPAR)

CDR Program Document Number: CDRP-ATBD-1451
Configuration Item Number: 01B-20c
Revision 0 / November 28, 2023

REVISION HISTORY

Rev.	Author	DSR No.	Description	Date
0	James Ray, SSAI/NASA	DSR-1853	Submission to CDR Program	11/07/2023

TABLE of CONTENTS

LIST of FIGURES

LIST of TABLES

1. Introduction

1.1 Purpose

The purpose of this document is to describe the algorithm submitted to the National Centers for Environmental Information (NCEI) by Dr. Eric Vermote, NASA/GSFC, Terrestrial Information Systems Branch, Code 619, that will be used to create the Leaf Area Index and Fraction of Absorbed Photosynthetically Active Radiation Climate Data Record (CDR) using the Visible Infrared Imager Radiometer Suite (VIIRS) sensors onboard the NPOESS Preparatory Project (NPP) spacecraft launched by the National Aeronautics and Space Administration (NASA) and the Joint Polar Satellite System (JPSS) launched jointly by the National Oceanic and Atmospheric Administration (NOAA) and NASA. The actual algorithm is defined by the computer program (code) that accompanies this document, and thus the intent here is to provide a guide to understanding that algorithm, from both a scientific perspective and in order to assist a software engineer or end-user performing an evaluation of the code.

1.2 Definitions

Following is a summary of the symbols used to define the algorithm.

θ_s = *sun zenith angle.* (1)

θ_v = *view zenith angle.* (2)

Φ = *view-sun relative azimuth.* (3)

ρ = *reflectance.* (4)

ξ = *scattering angle.* (5)

Fo = solar radiance. (6)

F_1 = *volume scattering kernel.* (7)

F_2 = *geometric kernel.* (8)

k0, k1, k2 = BRDF kernel coefficient. (9)

1.3 Referencing this Document

This document should be referenced as follows:

Leaf Area Index and FAPAR Climate Algorithm Theoretical Basis Document, NOAA Climate Data Record Program CDRP-ATBD-0564 Rev. 1 (2023). Available at https://www.ncei.noaa.gov/products/climate-data-records

1.4 Document Maintenance

Periodic updates to the algorithm and dataset are possible to occur. This could be (for example) when improvements to the algorithm are developed. Any update will be given a new version number, and an updated version of the C-ATBD will be generated.

2. Observing Systems Overview

2.1 Products Generated

The objective of this algorithm is to retrieve the Leaf Area Index (LAI) and the Fraction of Absorbed Photosynthetically Active Radiation (FAPAR) from VIIRS sensors. The final data set contains data from January 2014 to present. Additional quality information is provided such as cloud state and land cover class. Products are mapped into a daily 0.05°x0.05° grid, corresponding to a 3600x7200 array over the globe.

2.2 Instrument Characteristics

LAI and FAPAR products will be generated for each cloud-free pixel (0.05°x0.05°) observed by the VIIRS channels I1 and I2 as described in the VIIRS Surface Reflectance C-ATBD (CDRP-ATBD-1267). The current algorithm reads the channels from data similar to the VIIRS Surface Reflectance CDR dataset dataset: the BRDF-corrected VNP09CMG (for Suomi-NPP), VJ109CMG (for JPSS-1) and VJ209CMG (for JPSS-2) files. Timeline of the NPP/JPSS platforms is presented in Figure 1.

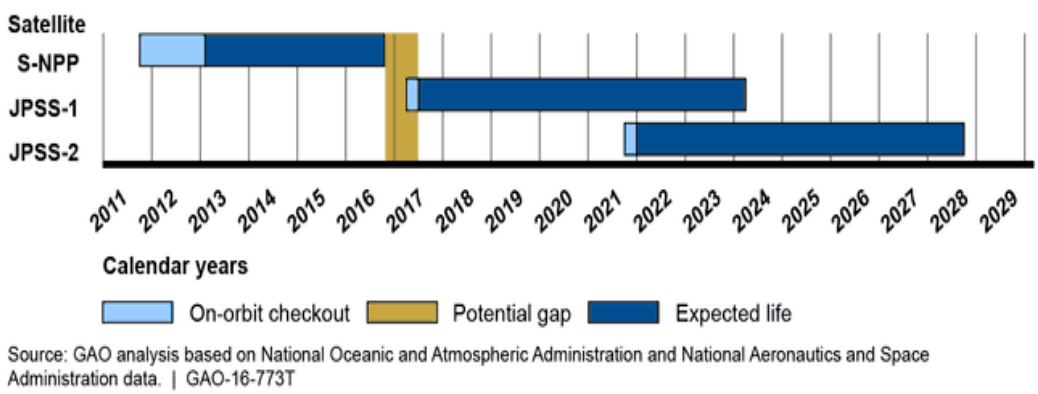

Figure 1: Timeline of the NPP/JPSS platforms as of 2016. (Today, all satellites are operational).

3. Algorithm Description

3.1 Algorithm Overview

This section aims to describe the algorithm at the current level of maturity (which will be updated with each revision). The algorithm includes retrieval of LAI and FAPAR from VIIRS channels I1 and I2.

3.2 Processing Outline

The processing outline of the VIIRS LAI / FAPAR processing is summarized in the Data Flow Diagram of Figure 2.

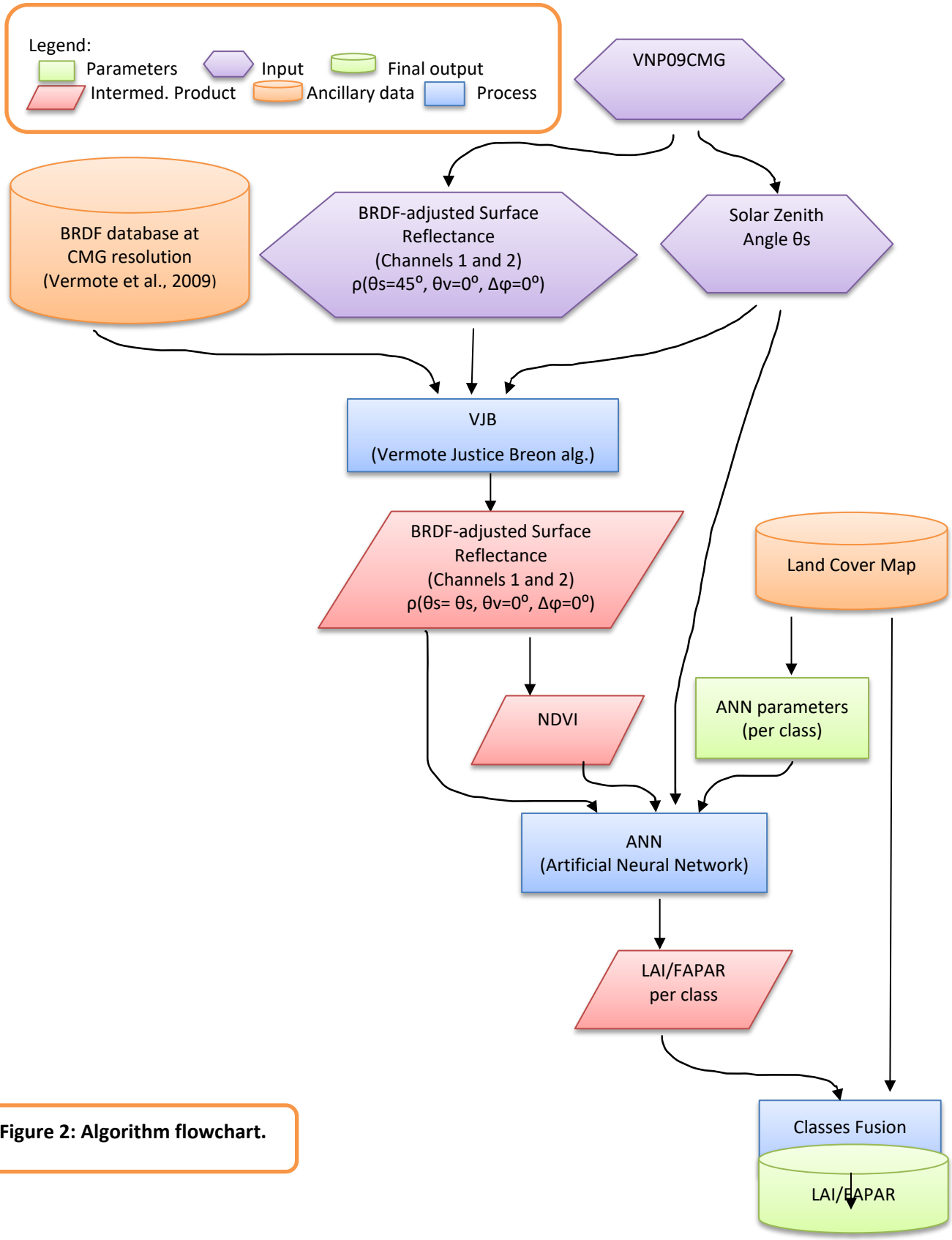

Figure 2: Algorithm flowchart.

3.3 Algorithm Input

3.3.1 Primary Sensor Data

Primary Sensor Data are Bidirectional reflectance distribution function (BRDF) adjusted surface reflectance data derived from VNP09CMG, VJ109CMG, and VJ209CMG products. Sun zenith angle is also used from the same products to retrieve the surface reflectance non-adjusted from the sun geometry. Data are described in Table 1.

Table 1: Primary Sensor Data

Name	Type	Description	Source	Dimension (spatial resolution)
surface reflectance (Channels 1, 2)	Input	BRDF-adjusted surface reflectance	VNP09CMG VJ109CMG VJ209CMG	0.05°
Sun zenith angle	Input	Sun zenith angle	VNP09CMG VJ109CMG VJ209CMG	0.05°

3.3.2 Ancillary Data

The LAI / FAPAR algorithm requires ancillary data listed in Table 2.

Table 2: Ancillary Data

Name	Type	Description	Source	Dimension (spatial resolution)
BRDF database	Ancillary	Pixel-based BRDF database of the VJB model	internal	0.05°
Land cover classification 1981-1994	Ancillary	IGBP* Land cover classification 1981-1994 from Hansen et al. (2000) resampled at 0.05°	Hansen et al. (1998)	0.05°

* International Geosphere-Biosphere Program

Land cover classification follows the IGBP (International Geosphere-Biosphere Program) labeling. The map was produced by Hansen et al. (1998) for the period 1981-1994. To avoid inconsistent land cover changing, the same classification is used for the entire data set. Moreover, to reduce the number of Artificial Neural Network (ANN) and spatial discontinuities, the number of classes were reduced from 17 to 6 (see Table 3).

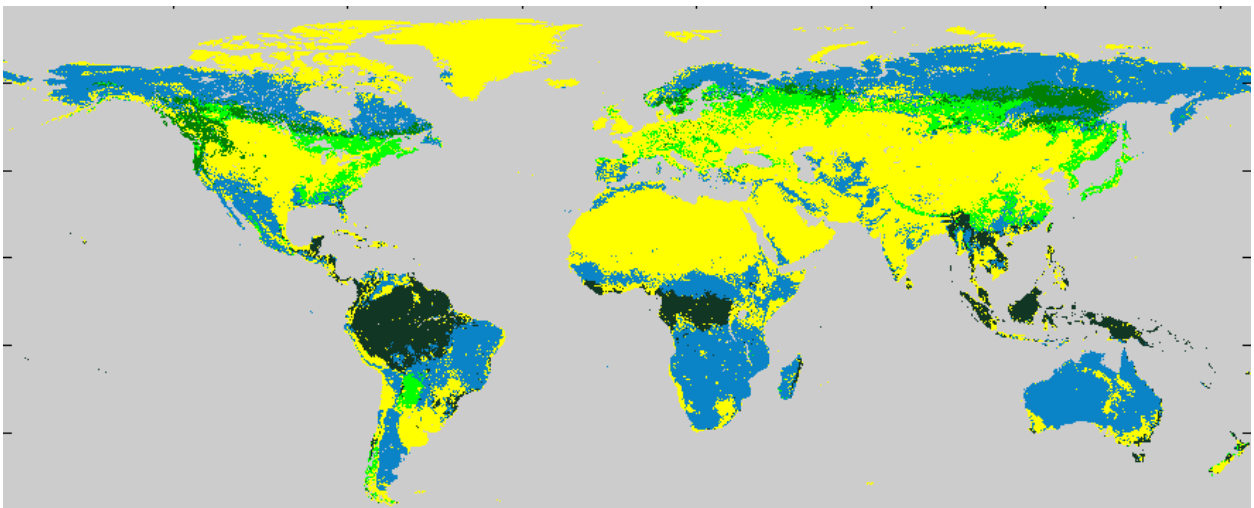

Figure 3: Landcover for year 2004. Grey: water; blue: shrubland; yellow: Grasslands & Croplands & Non vegetated; light green: broadleaf forest; green: needleleaf forest; dark green: evergreen broadleaf forest

Table 3: Reclassification table of the land cover classes

IGBP Class Name	Code	New Class Name	Code
water	0	water	6
evergreen needleleaf forest	1	needleleaf forest	1
evergreen broadleaf forest	2	evergreen broadleaf forest	5
deciduous needleleaf forest	3	needleleaf forest	1
deciduous broadleaf forest	4	broadleaf forest	2
mixed forests	5	broadleaf forest	2
closed shrublands	6	shrublands	3
open shrublands	7	shrublands	3
woody savannas	8	shrublands	3
savannas	9	shrublands	3
grasslands	10	grasslands, croplands & non-vegetated	4
permanent wetlands	11	grasslands, croplands & non-vegetated	4
croplands	12	grasslands, croplands & non-vegetated	4
urban and built-up	13	grasslands, croplands & non-vegetated	4
cropland/natural vegetation mosaic	14	grasslands, croplands & non-vegetated	4
snow and ice	15	grasslands, croplands & non-vegetated	4
barren or sparsely vegetated	16	grasslands, croplands & non-vegetated	4

3.3.3 Derived Data

<Not Applicable>

3.3.4 Forward Models

<Not Applicable>

3.4 Theoretical Description

In this section we describe the algorithms used to produce the LAI / FAPAR products.

3.4.1 Physical and Mathematical Description

3.4.1.1 VJB model

The VJB model (Vermote et al. 2009) is used to retrieve nadir-adjusted surface reflectance from BRDF- adjusted surface reflectance. The surface reflectance values of the VNP09CMG product are adjusted for the sun-view geometry to a constant view zenith angle (Θv=0°) and a constant sun zenith angle (Θs=45°). However, the FAPAR is a variable that varies according to the zenith angle. It is consequently more appropriate to derive FAPAR from nadir-adjusted surface reflectance keeping the original sun zenith angle through the implementation of the VJB, for which the theoretical basis is described below.

The analysis of Parasol multidirectional data has shown that, among analytical BRDF models, the Ross–Li–Maignan model provides the best fit to the measurements (Breon et al. 2012). This model computes the reflectance as the sum of three terms:

$$\begin{aligned}\rho(\theta_s,\theta_v,\phi) &= k_0 + k_1 F_1(\theta_s,\theta_v,\phi) + k_2 F_2(\theta_s,\theta_v,\phi)\\ &= k_0\left[1 + \frac{k_1}{k_0}F_1(\theta_s,\theta_v,\phi) + \frac{k_2}{k_0}F_2(\theta_s,\theta_v,\phi)\right]\end{aligned} \quad (10)$$

where F_1 is the volume scattering kernel, based on the Ross-thick function, but corrected for the Hot-Spot process, and F_2 is the geometric kernel, based on the Li-sparse reciprocal function. F_1 and F_2 are fixed functions of the observation geometry, but k_0, k_1, and k_2 are free parameters. In the following, we will use V as k_1/k_0 and R for k_2/k_0. The F_1 and F_2 functions are given in (11) and (12).

$$F_1(\theta_s, \theta_v, \varphi) = \frac{m}{\pi}(t - \sin t \cos t - \pi) + \frac{1 + \cos \xi}{2 \cos \theta_s \cos \theta_v}$$

$$\cos t = \frac{2}{m}\sqrt{\Delta^2 + (\tan \theta_s \tan \theta_v \sin \varphi)^2}$$

$$m = \frac{1}{\cos \theta_s} + \frac{1}{\cos \theta_v}$$

$$\Delta = \sqrt{tan(\theta_s)^2 + tan(\theta_v)^2 - 2 \times tan(\theta_s) \times tan(\theta_v) cos(\phi)} \quad (11)$$

$$F_2(\theta_s, \theta_v, \varphi) = \frac{4}{3\pi} \frac{1}{\cos \theta_s + \cos \theta_v} \left[\left(\frac{\pi}{2} - \xi\right) \cos \xi + \sin \xi\right]$$

$$\times \left(1 + \left(1 + \frac{\xi}{\xi_0}\right)^{-1}\right) - \frac{1}{3} \quad (12)$$

where ξ is the scattering angle and ξ_0 is a characteristic angle that can be related to the ratio of scattering element size and the canopy vertical density (ξ_0 =1.5°).

In VNP09CMG product, a correction of the directional effect is derived after transforming the measurement coordinates to standard observation geometry. The VNP09CMG standard observation geometry is for the Sun at 45° from zenith, and the observation at nadir. Therefore, the BRDF-adjusted (view and sun geometry) surface reflectance as used in VNP09CMG product is computed as eq (13), while the retrieval of the nadir-adjusted (view-geometry only) surface reflectance product is computed as eq (14).

$$\rho^N(45, 0, 0) = \rho(\theta_s, \theta_v, \phi)$$

$$\times \frac{1 + VF_1(45, 0, 0) + RF_2(45, 0, 0)}{1 + VF_1(\theta_s, \theta_v, \phi) + RF_2(\theta_s, \theta_v, \phi)} \quad (13)$$

$$\rho(\theta s, 0,0) = \rho^N(45,0,0) \times \frac{1+VF_1(\theta s,0,0)+RF_2(\theta s,0,0)}{1+VF_1(45,0,0)+RF_2(45,0,0)} \quad (14)$$

BRDF correction is based on pre-computed coefficients of V and R relationship with NDVI (Vermote et al. 2009).

V = V_slope * NDVI + V_intercep

R = R_slope * NDVI + R_intercep *(15)*

The 4 coefficients (V_slope, V_intercep, R_slope, R_intercep) were retrieved using the 2000-2011 MODIS archives following the approach presented in Vermote et al. (2009). Figure 4 illustrates V and R global maps derived from MODIS 2000-2004.

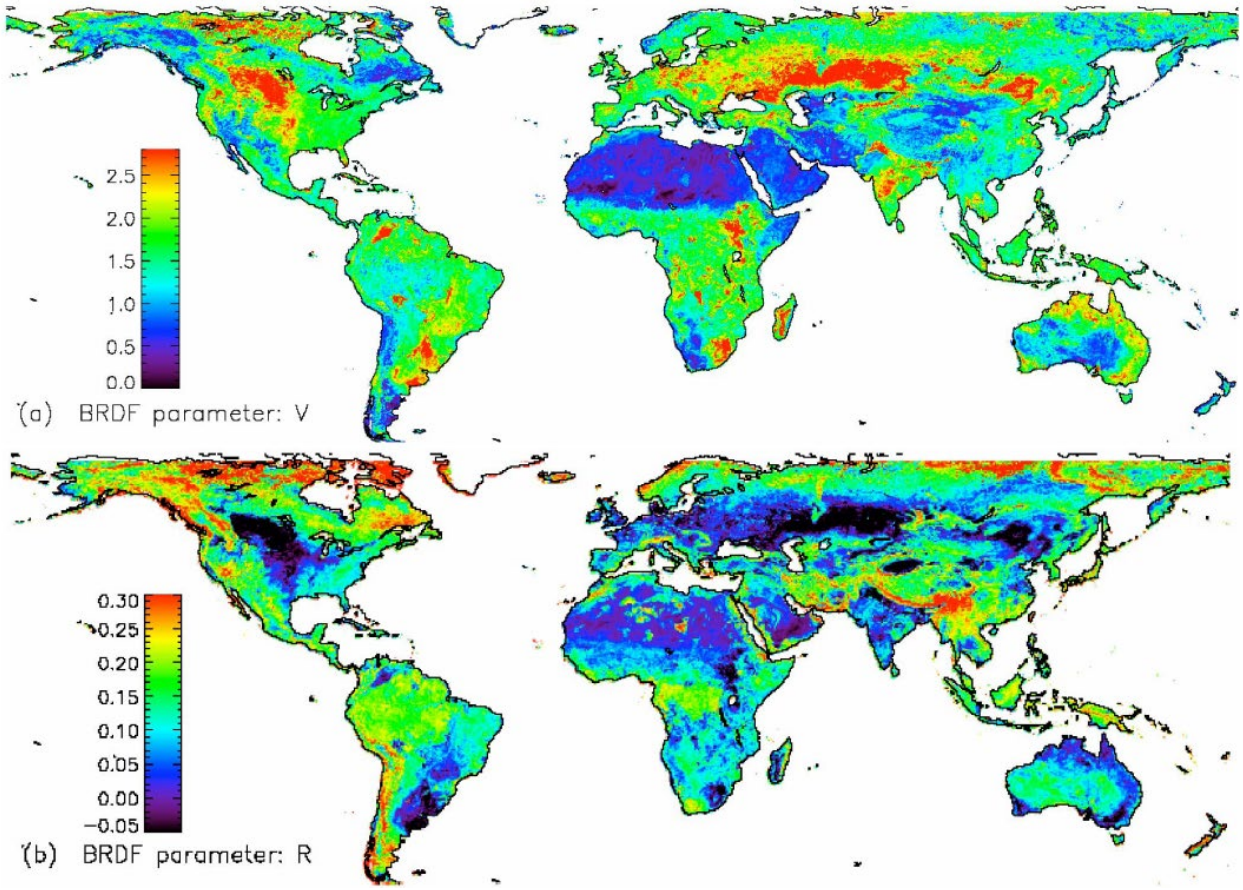

Figure 4: Global map of the V (a) and R (b) parameters derived by Vermote et al. (2009) applied to the time series of Terra MODIS band 2 (2000–2004). V and R are shown for highest NDVI values of each pixel.

3.4.1.2 Artificial Neural Network building

In this section, the methodology to derive the Artificial Neural Network (ANN) parameters used to relate nadir-adjusted surface reflectance to LAI and FAPAR is described. We used the MODIS product MCD15 as reference LAI and FAPAR values.

Note that VIIRS LAI/FAPAR is currently computed using ANN parameters derived from AVHRR data. These are the same parameters described in CDRP-ATBD-0564, the C-ATBD for AVHRR-derived LAI/FAPAR. We will here reproduce the relevant sections from the earlier C-ATBD (sections 3.4.1.2.1 ”Input/output dataset for the training of the ANN”, 3.4.1.2.2 “Domain definition”, and 3.4.1.2.3 “ANN training”).

3.4.1.2.1 Input/output dataset for the training of the ANN

AVH09C1 surface reflectance products

AVH09C1 products were selected from NOAA-16 during the year 2000-2007. A full description of the products is given in the AVHRR Surface Reflectance C-ATBD (CDRP-ATBD-0459). We retained pixel flag in the products as cloud, cloud-shadow and snow free. NDVI was derived directly from the nadir-adjusted surface reflectance.

MCD15 LAI/FAPAR products

The MCD15A2 (denoted MCD15 hereafter) is a global LAI and FAPAR product, composited every 8 days at 1-kilometer resolution on a Sinusoidal grid. Data were extracted for the period 2000-2007.

MODIS main algorithm is based on Look Up Tables (LUT) simulated from a three-dimensional radiative transfer model (Knyazikhin et al., 1998). Red and NIR atmospherically corrected MODIS reflectance (Vermote et al., 1997) and the corresponding illumination-view geometry are used as inputs of the LUT. The output is the mean LAI and FAPAR values computed over the set of acceptable LUT elements for which simulated and MODIS surface reflectances agree within specified level of (model and measurement) uncertainties. When the main algorithm fails, a backup algorithm based on NDVI (Normalized Difference Vegetation Index) relationships, calibrated over the same radiative transfer model simulations is used (Yang et al., 2006). We retained pixel flag as derived from the main algorithm and back-up algorithm.

FAPAR product corresponds to the instantaneous value at the time of the satellite overpass. LAI and FAPAR are first produced daily. Then, the 8 days composite corresponds to the values of the product when the maximum FAPAR value within the eight days period is observed. Note that no LAI and FAPAR values are retrieved over bare or very sparsely vegetated area, permanent ice or snow area, permanent wetland, urban area, or water bodies.

Sites selection

In order to limit the amount of processing data, a sample of globally distributed sites were selected. We used the BELMANIP-2 and DIRECT networks (Figure 5). Data were obtained

through the On LIne Validation Exercise (OLIVE) a CEOS/LPV initiative for on line validation of global land products (http://calvalportal.ceos.org/web/olive/).

BELMANIP2 (BEnchmark Land Multisite ANalysis and Intercomparison of Products) was built using sites from existing experimental networks (FLUXNET, AERONET, VALERI, BigFoot,...) completed with selected sites from the GLC2000 land cover map. BELMANIP2 was built using vegetation land cover map. The sites selection was performed for each band of latitude (10° width) by keeping the same proportion of biome types within the selected sites as within the whole band of latitude. Attention was paid so that the sites were homogeneous over a 10x10km^2 area, almost flat, and with a minimum proportion of urban area and permanent water bodies. The BELMANIP2 dataset included 445 sites.

DIRECT is a collection of sites for which ground measurements are available and that have been collected (Garrigues et al, 2008) and processed according to the CEOS-LPV guidelines. There are currently 113 data sets (sites and dates of measurements) available.

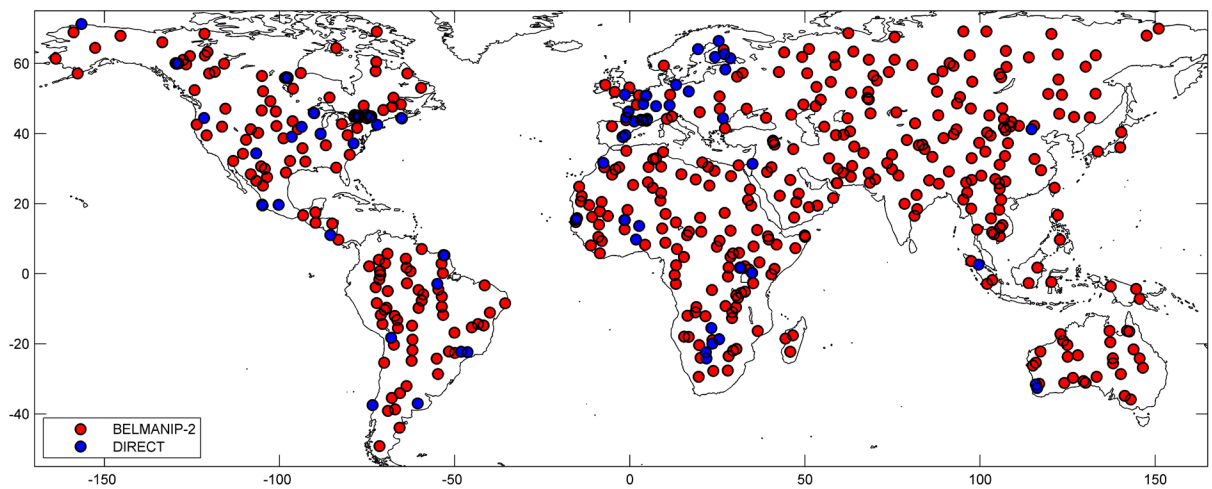

Figure 5: BELMANIP-2 and DIRECT network sites location.

<u>Spatial and temporal consideration</u>

We consequently extracted time series of MCD15 and AVH09C1 products over BELMANIP-2 and DIRECT sites. We focused on coincident years between AVHRR-NOAA-16 and MODIS products: 2001-2007.

MCD15 products are 1km resolution. We aggregate the product to the equivalent VNP09CMG product, i. e. 0.05°. MCD15 products are produced every 8 days. To limit the time series noise, we aggregate the product monthly. Same processing was done for VNP09CMG product.

3.4.1.2.2 Domain definition

ANN are trained over a defined area and their confidence considerably decrease out of the domain delimited by the learning dataset. The Domain definition was defined based on

NOAA-16 AVHRR Surface reflectance pixels corresponding to BELMANIP-2 sites for the 2001-2007 period.

Figure 6 represents the density distribution of the learning dataset of each class and the associated domain delimited by a polygon. Polygons were defined to include 97% of the density distribution pixels (0.01 resolution for rho1 and rho2). With these selected pixels, we used a convex hull algorithm to define an envelope polygon. Finally, the envelope was simplified using a Recursive Douglas-Peucker Polyline Simplification algorithm.

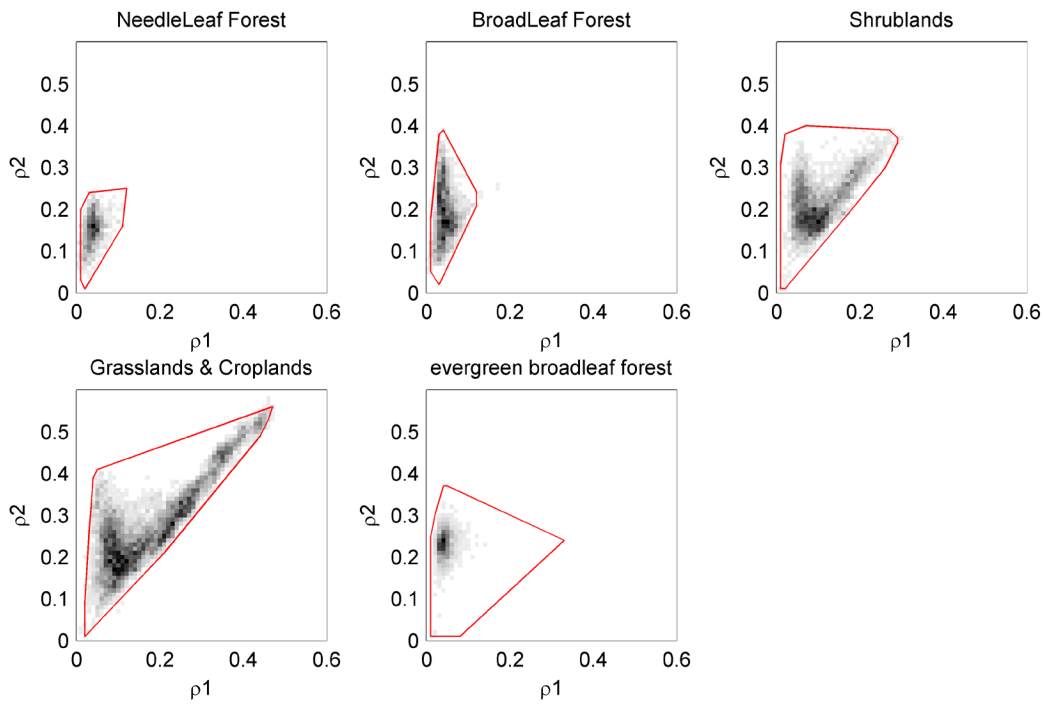

Figure 6: Domain definition for the 5 classes (red polygons). Grey images represent the density function for each 0.01 surface reflectance bin (white = no value; black = high density).

Each processed pixel is consequently compared to the polygon of the corresponding class. If it fits outside the polygon (bits described by "Polygon test" in Table 7), a flag is reported in the QA to show a lower confidence on the retrieval.

3.4.1.2.3 ANN training

ANN are a connection of neurons, associated by "synaptic" weights. Each neuron transforms the sum of the weighted signal from the previous neurons according to a given transfer function and a bias. The combination of sigmoid and linear functions is capable to fit any type of function (Demuth and Beale, 1998).

The training step is divided in 2 parts: Normalization of the inputs and outputs, ANN learning and de-normalization of the outputs.

Normalization is achieved simply by scaling between the minimum and maximum values: the normalized values, Y will vary between -1 and +1, and are computed from the raw values X and the minimum X_{min} and maximum X_{max} values (eq 16 and 17).

$$Y = \frac{2\times(X-X_{min})}{(X_{max}-X_{min})} - 1 \qquad (16)$$

$$X = \left({}^{1}/_{2} \times (X_{max} - X_{min}) \times (Y + 1)\right) + X_{min} \qquad (17)$$

Minimum and maximum values of input and outputs are presented in Table 4.

Table 4: Minimum and maximum values used for the normalization

Class	NeedleLeaf Forest		BroadLeaf Forest		Shrublands		Grasslands & Croplands & Non vegetated		evergreen broadleaf forest	
	Min	**Max**	**Min**	**Max**	**Min**	**Max**	**Min**	**Max**	**Min**	**Max**
rho1	0.01	0.11	0.01	0.12	0.01	0.29	0.02	0.42	0.01	0.31
rho2	0.02	0.24	0.04	0.39	0.01	0.39	0.02	0.48	0.01	0.37
cos(theta)	0.05	0.85	0.14	0.88	0.06	0.88	0.01	0.88	0.46	0.88
NDVI	0.01	0.86	-0.01	0.87	-0.22	0.92	-0.22	0.80	-0.41	0.91
LAI	0.00	5.24	0.01	5.94	0.00	5.95	0.00	5.27	0.69	6.72
FAPAR	0.01	0.93	0.02	0.92	0.00	0.89	0.00	0.89	0.23	0.91

Separate ANN were built for both output products LAI and FAPAR and each of the 5 classes as described in section 3.3.2. The ANN architecture finally retained followed the proposition of (Claverie et al. 2013) and are composed of (Figure 7):

- One input layer made of the 4 normalized input data.
- One hidden layer with 5 neurons having tangent sigmoid transfer functions.
- One output layer with a linear transfer function.

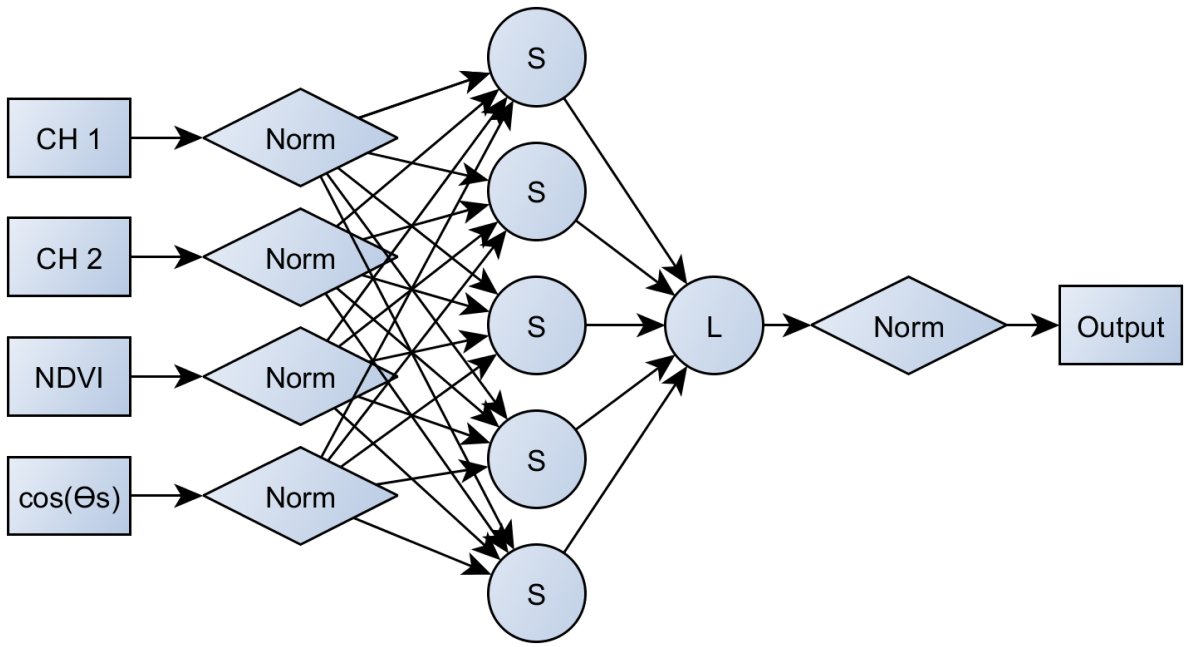

Figure 7: Conceptual representation of the Artificial Neural Network, including normalization steps. S and L stand for "sigmoid" and "linear" neurons, respectively; CH 1, 2 are reflectances in each channel (equivalent to rho1, rho2).

For each configuration (5 classes x 2 output variables), 10 ANN were trained, resulting to 100 ANN in total. The selection of the "optimal" ANN was based on the RMSE between the outputs and the "true" biophysical variables from sites used for validation (DIRECT network).

The learning process is mainly made of two elements: the training dataset that was described previously, and the learning rule that is now described. The Levenberg–Marquardt optimization algorithm is used to adjust the synaptic weights and neuron bias to get the best agreement between the output simulated by the network and the corresponding value of canopy biophysical variable simulated in the training data base. The initial values of the weights and biases were set to a random value between -1.0 and +1.0. Two networks are trained in parallel to retrieve LAI and FAPAR, each corresponding to independent random drawing of the initial values of the synaptic weights and bias.

3.4.1.3 Class Fusion

Maps corresponding to the five land cover types are fused according to the land cover maps described in section 3.3.2. The land cover is reported in the QA SDS.

3.4.2 Numerical Strategy

Artificial Neural Networks can model complex non-linear and multivariate systems with very simple output models. They include a set of coefficients for sigmoid and linear function and biases. ANN are very fast in computation and do not require any specific numerical strategy.

3.4.3 Calculations

The algorithm steps (see **Figure 2**) are the following:

- BRDF-adjustment via VJB model
- ANN application per class
- Class fusion.

They result in one NetCDF file including the following SDS:

- LAI
- FAPAR
- QA

3.4.4 Look-Up Table Description

<Not Applicable>

3.4.5 Parameterization

Parameterization of the ANN algorithm is defined in section 3.4.1.2.2. The sets of ANN coefficients for the 5 classes and the corresponding code and ANN parameterization are reported in the delivered code.

3.4.6 Algorithm Output

The output of the algorithm is one NetCDF file per day containing layers listed in Table 5. An example filename is:

VIIRS-Land_v001- NPP15C1_S-NPP_20230625_c20230627150204.nc

With the following naming convention:

<***product-name***> = static series name of the product with the value, “VIIRS-Land”

<***product-version***> = product version number, “v001”

<***product-type***> = NASA product type identifier with the valid domain:

"NPP15C1" = Suomi-NPP LAI/FAPAR; "JP115C1" = JPSS-1 LAI/FAPAR, etc.

<***sat-id***> = Source NPP/JPSS satellite ID with the valid domain:
"S-NPP", "NOAA-20", "NOAA-21"

<***YYYYmmdd***> = Date of the data in the file, formatted as year, month and day, with the valid range from "19810101" to present

c<***processing-date***> = Creation or processing date of the file identified with a 'c' followed by the year, month, day, hour, minute and second

.nc indicates the format (NetCDF)

Table 5: NPP15C1 output layers

Name	Description	Units	Dimension
crs	Latitude_longitude grid mapping	[-]	1
FAPAR	long_name = Fraction of Absorbed Photosynthetically Active Radiation	[-]	3600X7200
LAI	long_name = Leaf Area Index	$m^2.m^{-2}$	3600X7200
QA	long_name = Quality Assurance	[-]	3600X7200
longitude	long_name = longitude	degrees	7200
latitude	long_name = latitude	degrees	3600
lat_bnds	Top and bottom latitude of each grid cell	degrees	3600x2
lon_bnds	Top and bottom longitude of each grid cell	degrees	7200x2
time	long_name = time	days since 1981-01-01 00:00:00 UTC	1

4. Test Datasets and Outputs

4.1 Test Input Datasets

Note that VIIRS LAI/FAPAR is currently computed using ANN parameters derived from AVHRR data. These are the same parameters described in CDRP-ATBD-0564, the C-ATBD for AVHRR-derived LAI/FAPAR. We will here reproduce the relevant sections from the earlier C-ATBD (section 4.2, "Test Output Analysis"), with one additional section describing the algorithm's extension to VIIRS (4.2.4).

4.2 Test Output Analysis

4.2.1 Reproducibility

The evaluation of the reproducibility is done through the theoretical performance of the ANN. The 5 ANN related to the 5 land cover classes were trained based on MCD15 extraction over BELMANIP-2 sites. DIRECT sites were not used for the training but only for the evaluation of the ANN. Figures 8 (LAI) and 9 (FAPAR) display the theoretical performances of the ANN for the 5 classes.

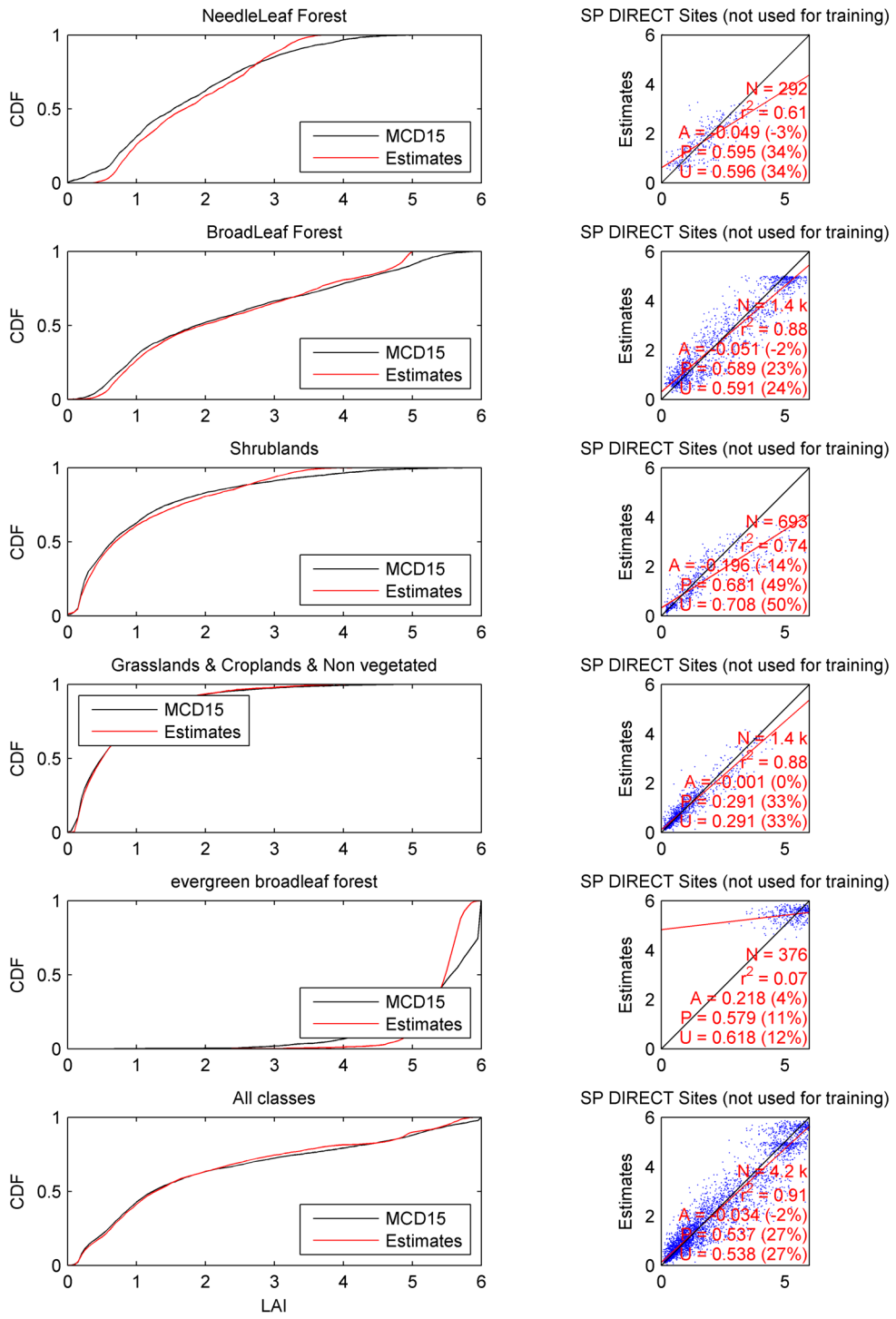

Figure 8: Theoretical performance of the LAI retrieval. Each line refers to a land cover class and last line to all classes merged. On the left subplots, the cumulative distribution function of input data for the training (i.e. MCD15) and output retrieval. On the right subplots, scatter plot between MCD15 (x-axis)

and Estimates (y-axis) are displayed. Only data for DIRECT sites (not used for training) were plotted. A, P and U corresponds to Accuracy, Precision and Uncertainty metrics (see Vermote and Kotchenova 2008 for more details).

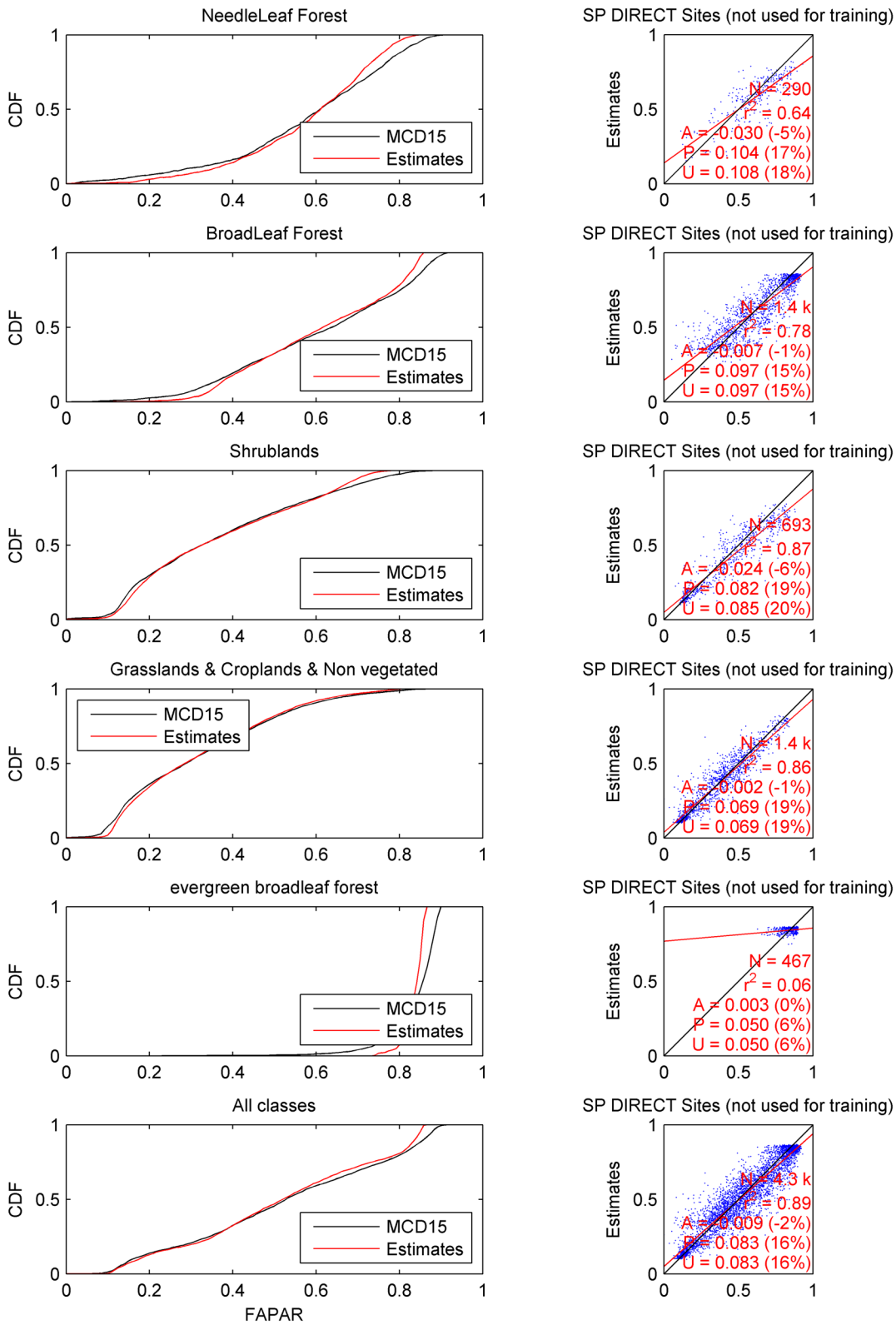
NeedleLeaf Forest
SP DIRECT Sites (not used for training)
N = 290
r² = 0.64
A = -0.030 (-5%)
P = 0.104 (17%)
U = 0.108 (18%)
BroadLeaf Forest
SP DIRECT Sites (not used for training)
N = 1.4 k
r² = 0.78
A = -0.007 (-1%)
P = 0.097 (15%)
U = 0.097 (15%)
Shrublands
SP DIRECT Sites (not used for training)
N = 693
r² = 0.87
A = -0.024 (-6%)
P = 0.082 (19%)
U = 0.085 (20%)
Grasslands & Croplands & Non vegetated
SP DIRECT Sites (not used for training)
N = 1.4 k
r² = 0.86
A = -0.002 (-1%)
P = 0.069 (19%)
U = 0.069 (19%)
evergreen broadleaf forest
SP DIRECT Sites (not used for training)
N = 467
r² = 0.06
A = 0.003 (0%)
P = 0.050 (6%)
U = 0.050 (6%)
All classes
SP DIRECT Sites (not used for training)
N = 4.3 k
r² = 0.89
A = -0.009 (-2%)
P = 0.083 (16%)
U = 0.083 (16%)
MCD15
Estimates
CDF
Estimates
FAPAR

Figure 9: Theoretical performance of the FAPAR retrieval. Refer to legend of Figure 8 for more details.

Another way to evaluate the reproducibility is to compare outputs from AVHRR sensors on board two different platforms. We selected NOAA-16 and NOAA-18 with an overlapping period from 02-Jul-2005 to 31-Dec-2006. The analysis is carried on BELMANIP-2 and DIRECT sites. The scatterplot is displayed in 10 and uncertainties are 0.35 for LAI and 0.08 for FAPAR.

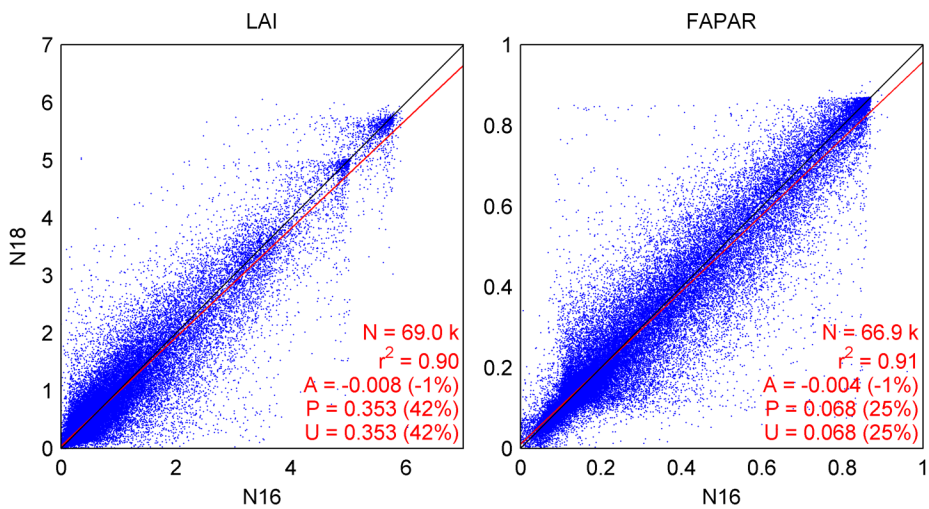

Figure 10: Comparison of retrieval from AVHRR-NOAA-16 (N16) and AVHRR-NOAA-18 (N18) for BELMANIP-2 and DIRECT sites from 02-Jul-2005 to 31-Dec-2006.

4.2.2 Precision and Accuracy

The performances of the estimates were evaluated over in situ measurements from the DIRECT network; the sites were not used in the learning process. Scatter plot per class are shown in Figure 11. LAI validation scatter plots were divided among the type of measurement: Effective and true LAI, depending if the clumping factor is included or not (see Claverie et al. 2012).

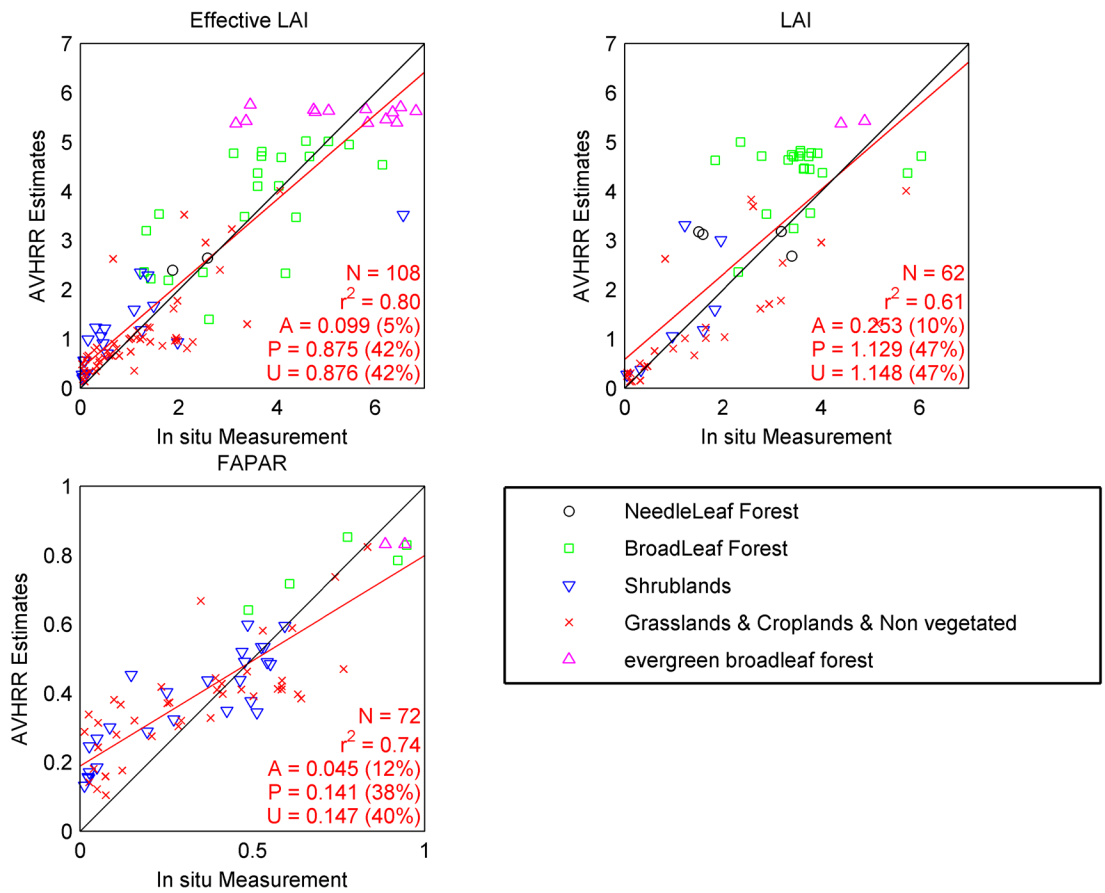

Figure 11: In-situ validation over DIRECT sites. Ground measurement covers initially a footprint of 3x3 km. they were extrapolated to 0.05° using MCD15 products.

4.2.3 Error Budget

The error budget is summarized in Table 6, which includes uncertainty, precision and accuracy from the validation over DIRECT sites.

Table 6: Error budget based on in-situ validation

Class	Effective LAI				True LAI				FAPAR			
	A	P	U	N	A	P	U	N	A	P	U	N
NeedleLeaf Forest	0.29	0.32	0.37	2	0.62	1.18	1.19	4				0
BroadLeaf Forest	0.28	1.03	1.05	22	0.81	1.02	1.29	22	0.02	0.13	0.12	5
Shrublands	0.2	0.9	0.9	20	0.4	0.88	0.91	7	0.07	0.12	0.13	25
Grasslands & Croplands & Non vegetated	-0.08	0.65	0.65	51	-0.33	1.07	1.1	27	0.04	0.16	0.16	40
evergreen broadleaf forest	0.14	1.35	1.31	14	0.76	0.3	0.79	2	-0.08	0.04	0.09	2
All	**0.08**	**0.89**	**0.89**	**109**	**0.25**	**1.13**	**1.15**	**62**	**0.05**	**0.14**	**0.15**	**72**

4.2.4 Extension to VIIRS

VIIRS LAI/FAPAR is currently computed using ANN parameters derived from AVHRR data. Data was run for years 2013 to 2017, comparing AVHRR LAI/FAPAR derived from NOAA-19 and VIIRS LAP/FAPAR from NOAA-20 (VNP). The scatter plots shown in figure 12 show LAI and FAPAR values at BELMANIP-2 sites, 2013 only, for all five biomes combined, for LAI (top, N = 28283) and FAPAR (bottom, N = 27913). Linear curve fitting demonstrated a r^2 value of 0.95 for LAI and 0.94 for FAPAR.

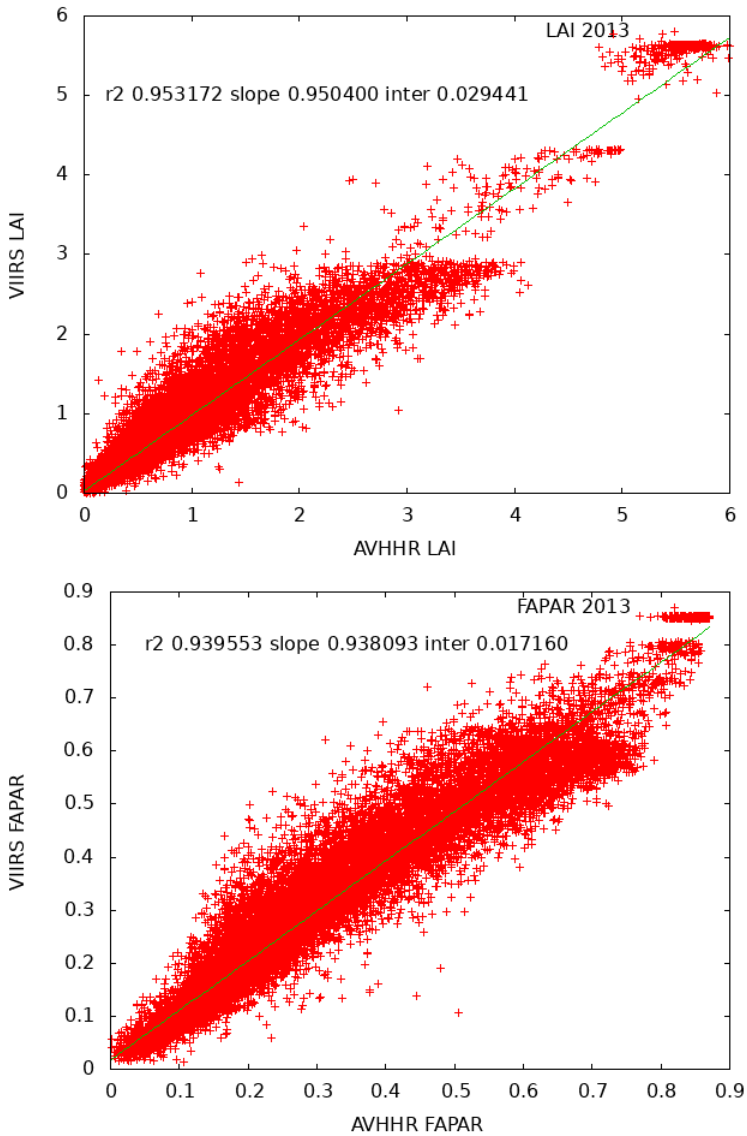

Figure 12: Continuity of VIIRS and AVHRR (N19) LAI (top) and FAPAR (bottom).

5. Practical Considerations

5.1 Numerical Computation Considerations

No parallelization or difficulties in matrix inversions are expected. The algorithm implementation is based on ANN to increase computation speed.

5.2 Programming and Procedural Considerations

<Not Applicable>

5.3 Quality Assessment and Diagnostics

The estimate of the LAI/FAPAR is accompanied with quality assurance information. QA bits contain information stored at the product resolution. The Table 7 describes the bit ordering to use the Quality Assessment SDS.

Table 7: QA SDS bits description. Bits are listed from the MSB (bit 7) to the LSB (bit 0). Optimal results may be obtained from data in polygon, BRDF-corrected and highest quality ("OK", cloud-free).

Bits Number	Bits Description	
6-7	Polygon test	00: in polygon
		01: not in polygon
		10: not tested (water/cloudy)
5	BRDF corrected	0: no
		1: yes
2-4	Associated Class	001: NeedleLeaf Forest
		010: BroadLeaf Forest
		011: Shrublands
		100: Grasslands & Croplands & Non vegetated
		101: Evergreen broadleaf forest
		110: Water
0-1	Quality control	00: OK
		01: Input flag as Cloudy
		10: Invalid input
		11: Output out of range

5.4 Exception Handling

<Not applicable>

5.5 Algorithm Validation

The C code was compared with the original Matlab code over a random data test of 1000 sample and the full image of day 142-2003.

5.6 Processing Environment and Resources

The CDR code is run on an 8-core 2.5GHz 64-bit Xeon server, running Ubuntu Linux 5.9 x86_64. The code was compiled with C-compiler GCC 4.4.7. The main C-libraries were: HDF5 8.88, HDF 4.2r4, NetCDF 4.2, Zlib 1.2, szip. A 10-year data set was processed in 25 hours.

6. Assumptions and Limitations

The main limitation of the algorithm is the capacity to reproduce LAI/FAPAR dynamic over Evergreen Broadleaf forest. This is due to a saturation of VIIRS Channel 1 and 2 signals over dense vegetation cover.

7. Future Enhancements

7.1 Land Cover map update

Land cover maps for future years will be based on the MCD12C1 product that can be found using this link: https://e4ftl01.cr.usgs.gov/MOTA/MCD12C1.061/

7.2 Improvement of the algorithm for broadleaf forest

As currently used, the algorithm is not capable of reproducing a consistent spatiotemporal LAI/FAPAR retrieval over evergreen broadleaf forest, and displays some saturation over broadleaf forest. Future work will be focused on algorithm enhancement.

8. References

Breon, F.-M., & Vermote, E. (2012). Correction of MODIS surface reflectance time series for BRDF effects. Remote Sensing of Environment, 125, 1-9

Claverie, M., Demarez, V., Duchemin, B., Hagolle, O., Ducrot, D., Marais-Sicre, C., Dejoux, J.-F., Huc, M., Keravec, P., Béziat, P., Fieuzal, R., Ceschia, E., & Dedieu, G. (2012). Maize and sunflower biomass estimation in southwest France using high spatial and temporal resolution remote sensing data. Remote Sensing of Environment, 124, 844-857.

Claverie, M., Vermote, E.F., Weiss, M., Baret, F., Hagolle, O., & Demarez, V. (2013). Validation of coarse spatial resolution LAI and FAPAR time series over cropland in southwest France. Remote Sensing of Environment, 139, 216-230

Demuth, H., & Beale, M. (1998). Neural network toolbox (for use with MATLAB). Natick, MA: The MathWorks Inc.

Garrigues, S., Lacaze, R., Baret, F., Morisette, J.T., Weiss, M., Nickeson, J.E., Fernandes, R., Plummer, S., Shabanov, N.V., Myneni, R.B., Knyazikhin, Y., & Yang, W. (2008). Validation and intercomparison of global Leaf Area Index products derived from remote sensing data. Journal of Geophysical Research-Biogeosciences, 113, G02028.

Hansen, M., R. DeFries, J.R.G. Townshend, and R. Sohlberg (1998), UMD Global Land Cover Classification, 1 Kilometer, 1.0, Department of Geography, University of Maryland, College Park, Maryland, 1981-1994.

Hansen, M., R. DeFries, J.R.G. Townshend, and R. Sohlberg (2000), Global land cover classification at 1km resolution using a decision tree classifier, International Journal of Remote Sensing. 21: 1331-1365.

Knyazikhin, Y., J. V. Martonchik, R. B. Myneni, D. J. Diner, and S. W. Running (1998), Synergistic algorithm for estimating vegetation canopy leaf area index and fraction of absorbed photosynthetically active radiation from MODIS and MISR data, J. Geophys. Res., 103(D24), 32,257 – 32,275.

Vermote, E., Justice, C.O., & Breon, F.M. (2009). Towards a Generalized Approach for Correction of the BRDF Effect in MODIS Directional Reflectances. Ieee Transactions on Geoscience and Remote Sensing, 47, 898-908.

Vermote, E.F., & Kotchenova, S. (2008). Atmospheric correction for the monitoring of land surfaces. Journal of Geophysical Research-Atmospheres, 113, D23S90

Vermote, E.F., D. Tanré, J.-L. Deuzé, M. Herman, J.-J. Morcrette (1997). Second Simulation of the Satellite Signal in the Solar Spectrum, 6s: An Overview. IEEE TRANSACTIONS ON GEOSCIENCE AND REMOTE SENSING, 35, 675-686

Yang, W., et al. (2006b), MODIS leaf area index products: From validation to algorithm improvement, IEEE Trans. Geosci. Remote Sens., 44(7), 1885 – 1898

Appendix A. Acronyms and Abbreviations

Acronym or Abbreviation	Definition
ANN	Artificial Neural Network
AVHRR	Advanced Very High Resolution Radiometer
BELMANIP	BEnchmark Land Multisite ANalysis and Intercomparison of Products
BRDF	Bidirectional reflectance distribution function
C-ATBD	Climate Algorithm Theoretical Basis Document
CDR	Climate Data Record
CEOS	Committee on Earth Observation Satellites
CMG	Climate Modelling Grid
DIRECT	Sites at which LAI ground truth values were determined in early studies (see https://ieeexplore.ieee.org/document/1645280)
FAPAR	Fraction of Absorbed Photosynthetically Active Radiation
HDF	Hierarchical Data Format
IEEE	Institute of Electrical and Electronic Engineers
IGBP	International Geosphere-Biosphere Program
LAI	Leaf Area Index
LPV	Land Product Validation
LSB	Least Significant Bit
LUT	Look Up Tables
MODIS	Moderate Resolution Imaging Spectroradiometer
MSB	Most Significant Bit
NCEI	National Centers for Environmental Information
NDVI	Normalized Difference Vegetation Index
NIR	Near infrared
NOAA	National Oceanic and Atmospheric Administration
OLIVE	On Line Validation Exercise
QA	Quality Assessment
RMSE	Root-mean-square error
SDS	Science Data Sets
VIIRS	Visible Infrared Imager Radiometer Suite
VJB	Vermote Justice Breon